Fusion and interaction barrier parameters and critical angular momenta from ^{35}Cl-induced reactions*

W. Scobel
Nuclear Structure Research Laboratory,† University of Rochester, Rochester, New York 14627 and Fachbereich Physik, Universität Hamburg, Hamburg, Germany

H. H. Gutbrod‡
Gesellschaft für Schwerionenforschung, Darmstadt, Germany

M. Blann and A. Mignerey
Nuclear Structure Research Laboratory,† University of Rochester, Rochester, New York 14627

(Received 11 June 1976)

Cross sections for evaporation residue formation and fission following complete fusion of ^{35}Cl with ^{27}Al, ^{48}Ti, ^{54,56}Fe, ^{58,60,62,64}Ni, ^{90}Zr, and ^{116,124}Sn have been measured with counter telescopes for laboratory projectile energies between 70 and 170 MeV. Elastic scattering of ^{35}Cl + ^{58,62}Ni has been measured near the interaction barrier. The excitation functions for complete fusion are analyzed with a semiclassical model, and fusion barrier heights and radii are extracted. These data are discussed in terms of the nuclear density overlap and the nuclear potential contributions to the fusion barrier. The results are compared with the predictions of several heavy ion potential models and with parameters for the interaction deduced from elastic scattering data. For the systems with masses $A < 100$ about 70% of the total reaction cross section appears as complete fusion. This fraction decreases with increasing mass of the compound system. Evaporation residue and fission excitation functions have been analyzed by the Bohr-Wheeler model using the rotating liquid drop model of Cohen, Plasil, and Swiatecki. To first order these calculations give a satisfactory description of both sets of results.

[NUCLEAR REACTIONS ^{27}Al, ^{48}Ti, ^{54,56}Fe, ^{58,60,62,64}Ni, ^{90}Zr, ^{116,124}Sn (^{35}Cl, X), E_{lab} = 70–170 MeV; measured $\sigma(E,\Theta)$, $\sigma_{EL}(\Theta)$, σ_{CF}, σ_{FISS}; deduced fusion barrier heights, radii, critical angular momenta.]

I. INTRODUCTION

The mechanisms of heavy ion interactions, and in particular, the dynamics of compound nucleus formation have attracted the interest of experimentalists and theoreticians in recent years. Corresponding studies have been stimulated by a new generation of upgraded tandem accelerators and the variety of heavy ion beams available, and by the increasing number of microscopic and phenomenological nuclear potentials proposed for the description of the reactions between heavy ions.[1-16]

In this work we present measurements on the interaction of ^{35}Cl with target nuclei in the mass range A = 27–124. Projectile energies varied between 70 and 170 MeV. The data primarily consist of differential cross sections for evaporation residue formation. Elastic scattering of ^{35}Cl + ^{58,62}Ni has been measured near the interaction threshold. The onset of fission-like processes could be observed for the systems ^{35}Cl + ^{48}Ti, ^{62}Ni, and ^{116,124}Sn. From these data, excitation functions for compound nucleus formation are derived to yield fusion barrier heights and radial positions in the sharp cutoff approximation as well as critical angular momenta.

It was our goal not to study one single system extensively, but to get a consistent set of data constituting a survey over a broad range of target nuclei. On the basis of these experimental results and additional information from the literature we try to contribute to the answers for the following questions:

(i) What is the general dependence of the fusion barrier parameters on the target and projectile masses and charges involved and to what extent do isotopic sequences of nuclei, e.g., ^{35}Cl + ^{58,60,62,64}Ni, deviate from this average trend?
(ii) What fraction of the reaction cross section goes into complete fusion and how do fusion and interaction barrier parameters compare?
(iii) Are the heavy ion potential models under discussion able to reproduce the fusion barrier parameters and complete fusion cross sections?
(iv) What can be learned from the angular momentum limits for compound nucleus formation and the onset of evaporation residue/fission competition and what are the predictions of the compound nucleus evaporation theory including

angular-momentum-dependent fission?[17]

In the following section we present a short description of the experimental technique. In Sec. III the experimental results are given. Section IV is devoted to the interpretation of these data and comparisons with model calculations in context with the questions raised above.

II. EXPERIMENTAL PROCEDURE

The experiments were performed with the analyzed ^{35}Cl beam provided by the Rochester MP tandem Van de Graaff and the three stage MP tandem facility at Brookhaven National Laboratory. The projectile energies in the laboratory frame varied between 70 and 170 MeV. The lower energies were achieved in two stage operation with 8^+–11^+ projectile charge state, whereas the highest energies required three stage operation and double foil stripping[19] up to charge state 14^+. Typical (particle) beam intensities varied between 100 pA (10 pA) and 100 nA (10 nA). The lower intensity beams were either necessary for small reaction angle runs or given by the maximum yield of the accelerator facility at the highest energies attainable. The different types of reaction products are identified by means of energy, energy loss, and angular distributions.

The features of the targets used are listed in Table I. Angular distributions of evaporation residues, elastically scattered ^{35}Cl ions, recoil nuclei and, in some cases, direct transfer and fission products were detected in 60–80 cm diameter scattering chambers by two telescopes, each consisting of a ΔE gas proportional counter and a $(E - \Delta E)$ silicon surface barrier detector with 1 mm × 4 mm entrance apertures. Two solid state detectors at fixed angles of 10°–20° on either side of the projectile beam direction were used for monitoring purposes and control of the beam position on target. The telescope angles were thus defined to better than 0.2°. Further details of the experimental setup and techniques are given in Refs. 3 and 4. A typical spectrum obtained with these telescopes is shown in Fig. 1. The experimental 128 × 128 channel setup is reduced to a 64 × 64 array for this presentation and is supplemented by a contour plot.

The absolute differential cross sections were derived by normalizing the relative cross sections to the simultaneously measured elastic scattering in those angular regions where the scattering was found to be Rutherford in character within the uncertainties of this experiment. Thus uncertainties in the absolute cross sections arising from target thickness, beam current integration, and counter dead time, are avoided.

III. RESULTS

A. Elastic scattering

The elastic scattering was intensively measured at 100 MeV for ^{35}Cl on ^{58,62}Ni, i.e., near the fusion barrier of the colliding systems.[4] The angular distributions normalized to the Rutherford cross sections are shown in Fig. 2. An optical model fit, starting from a standard parameter set[18] has been performed. The resulting parameters and the fit are also given in Fig. 2. The optical model analysis yields total reaction cross sections of 83 and 182 mb for ^{35}Cl on ^{58,62}Ni, respectively.

For ^{35}Cl on ^{62}Ni at 100 MeV it was possible to separate and identify the heavy transfer reaction products. Their angular distribution is also shown in Fig. 2; it shows a peak at the position of the grazing angle. From this distribution the total transfer reaction cross section could be estimated to $\sigma_{tr} = 23 \pm 8$ mb.

B. Evaporation residues

Events that arise from fusion with subsequent evaporation of some nucleons and/or light clusters

TABLE I. Targets used in this work.

Target	^{27}Al	^{48}Ti	^{54}Fe	^{56}Fe	^{58}Ni	^{60}Ni	^{62}Ni	^{64}Ni	^{90}Zr	^{116}Sn	^{124}Sn
Thickness (μg/cm^2)	50,100	50	175	50	60	40	50,100	70	35,60	175	110
Thickness [a] (keV)	800	650	1800	500	680	460	570	800	320	1400	880
Backing [b] (μg/cm^2)	ss	C 20	ss	C 20	ss	ss	ss	ss	C 20	ss	ss
Isotopic purity [c]	>99.9	98	>91	99.8	99.9	99.8	98.8	98.0	97.8	96.8	88

[a] Calculated for ^{35}Cl projectiles at the fusion threshold.
[b] ss: self-supporting. C 20: 20 μg/cm^2 carbon backing.
[c] Purity of the material used for target production.

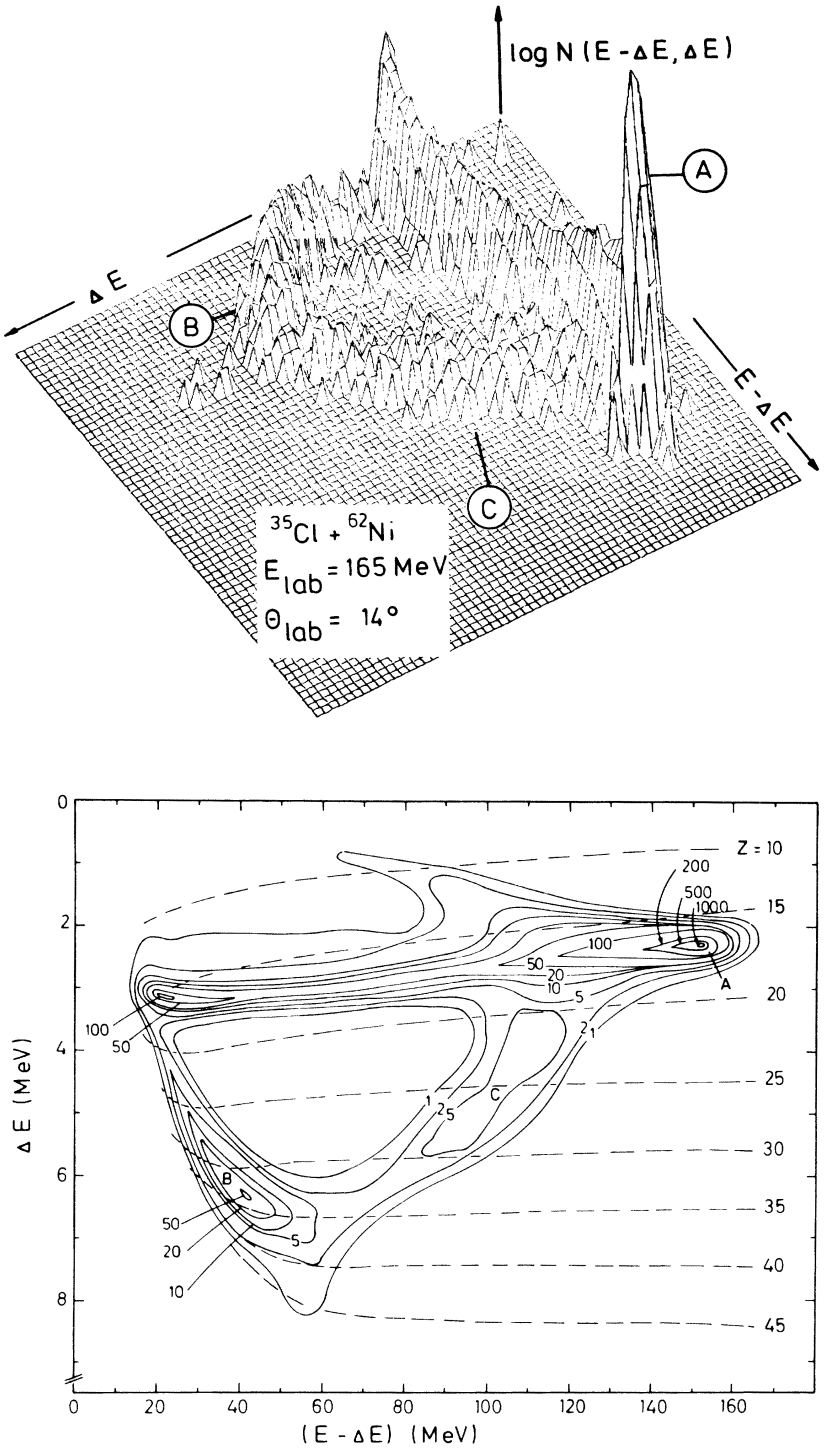

FIG. 1. Isometric display and contour diagram of ΔE vs $(E-\Delta E)$ spectrum for 165 MeV $^{35}Cl+^{62}Ni$ at $\Theta_{lab}=14°$. In the isometric display the intensity scale is logarithmic; elastic scattering (A), evaporation residues (B), and a broad distribution of fission-like events (C) can be distinguished. The solid contours in the lower part represent the intensity of reaction products. The dashed lines indicate the average positions of the charge numbers Z. The calibration of the ΔE vs $(E-\Delta E)$ plane with respect to Z was performed as presented in Refs. 6 and 22.

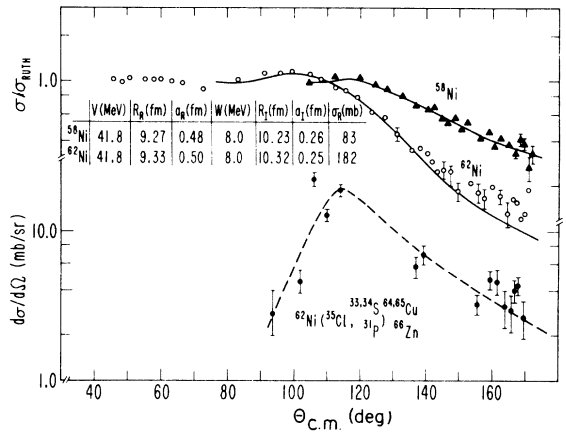

FIG. 2. Angular distributions for elastic scattering of ^{35}Cl at E_{lab}=100 MeV on ^{58}Ni and ^{62}Ni. The solid lines are the optical model fits with the parameter sets given. The Coulomb radius parameter used was r_0=1.35 fm. The quarter point method yields $\sigma_R(\Theta_{1/4})$=109 mb for ^{35}Cl+^{62}Ni. Also given the angular distribution of the heavy transfer products peaking around the grazing angle. Integration following the dashed line yields 23±8 mb.

are clearly separated from transfer- and fission-like events in the ΔE vs $(E-\Delta E)$ spectra (see Fig. 1) for all projectile energies and systems under study but ^{35}Cl+^{27}Al at the highest energies $E_{lab} \geq 160$ MeV. The angular distributions for evaporation residue formation therefore can be derived by integration of the number of heavy residues over angle. The atomic numbers of events considered as heavy residues are greater than those of the projectile by typically at least 4–5 units, see Fig. 1; furthermore, the residues occur with kinetic energies and angular distributions which preclude significant fission contributions, even for ^{35}Cl+^{27}Al at projectile energies $E_{lab} \geq 160$ MeV, where the separation by kinetic energies is ambiguous.

Data were taken for angles $\Theta_{lab} \geq 2.8°$, mostly in 1° or 2° steps. A representative selection of the resulting angular distributions for ^{35}Cl on ^{27}Al, ^{48}Ti, ^{54}Fe, ^{62}Ni, ^{90}Zr, and ^{116}Sn is shown in Fig. 3. Similar sets were obtained for ^{35}Cl on ^{56}Fe, ^{58,60,62,64}Ni, and ^{124}Sn. The angular distributions shown represent about 40% of all distributions taken in the course of this study. Part of the ^{35}Cl+Ni data have already been presented in Ref. 4.

It may be seen that the angular distributions are strongly forward peaked due to the low off axis momentum transfer from light particle evaporation and to multiple scattering in the target. These momentum transfers, however, are smaller the heavier the system, as is demonstrated in Fig. 4 with the evaporation residue angular distributions for ^{35}Cl on ^{27}Al, ^{62}Ni, and ^{116}Sn at energies comparable in residue yield.

The total evaporation residue cross sections σ_{ER} are derived from the angular distributions by integration. This requires an extrapolation of the data into the 0°–2.8° region. The extrapolations performed are consistent with the few lower angle evaporation residue data from track detector[7] and telescope[3] measurements. The resulting smoothed out angular distributions are shown in Fig. 3. Integration of these curves yields the evaporation residue cross sections listed in Table II. Due to the low solid angle weighting the contributions from the 0°–3° region vary between 20 and 40% as may be seen from Fig. 4. The shape chosen for extrapolation may introduce a systematic error in the absolute cross sections of the order of 5%. However, for one projectile-target combination, the experimental data presented in Fig. 4 show only a weak dependency of the angular distribution shape on the projectile energy, and there is no physical reason for assuming a much more pronounced change in the 0°–3° region. The extrapolation procedure chosen therefore will not affect the relative excitation functions $\sigma_{ER}(E)$. The relative errors given in Table II differ from absolute ones by this systematic uncertainty, so that an accuracy of 7–10% can be stated whenever the relative errors are 5–7%.

C. Fission

For the reactions ^{35}Cl on ^{48}Ti, ^{54,56}Fe, ^{62}Ni, and ^{116,124}Sn at the highest projectile energies reaction products have been observed that show a kinetic energy distribution consistent with the empirical formula of Viola[21] for the average kinetic energy of fission fragments, if the combined systems are assumed to undergo fission. These fission-like events have been integrated and their angular distributions have been converted into the center of mass system with the assumption of symmetric binary fission. Most of these data are restricted to forward angles $\Theta_{c.m.} \leq 50°$, but for measurements on ^{35}Cl+^{116,124}Sn data from this study and from Ref. 22 extend to backward angles. The angular distributions are shown in Fig. 5 together with $1/\sin\Theta_{c.m.}$ curves which represent the expected shape of angular distributions of fission products from highly rotating systems.[23] The measured angular distributions are not incompatible with fission of an equilibrated system, since there is no indication of a strong asymmetry around 90°. Therefore the angular distributions have been integrated under the assumption of an

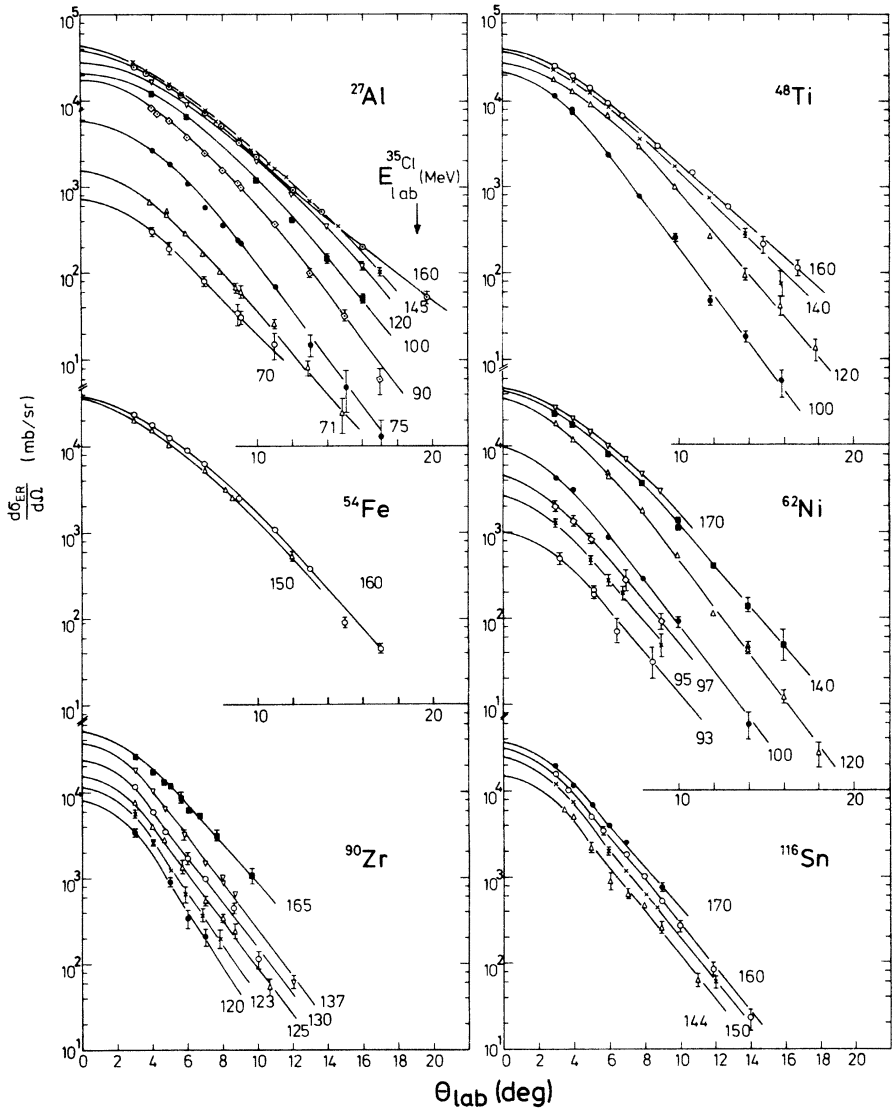

FIG. 3. Representative sets of angular distributions of the evaporation residues for different targets and projectile energies. Integrations were performed over the smoothed out distributions (solid lines).

$1/\sin\Theta_{c.m.}$ dependence, yielding the fission cross sections of Table II. For the system ^{35}Cl + ^{27}Al fission-like events were observed for projectile energies above 160 MeV, but could not be separated quantitatively from the evaporation residues due to their broad distribution in the ΔE vs $(E - \Delta E)$ spectrum. Therefore these events have been included in the determination of the evaporation residue cross section. It has been shown in a time-of-flight coincidence experiment,[5] that at 170 MeV projectile energy the fission contribution is still small compared with the evaporation residue formation; nevertheless, at higher angles $\sigma_{ER}(\Theta)$ and $\sigma_{FISS}(\Theta)$ become comparable because of their very different angular dependence. This explains the deviation of the angular distribution shape for ^{35}Cl + ^{27}Al at 160 MeV (Fig. 3) from that of the lower projectile energy runs. Further discussion concerning these fission-like contributions is given in the next section and in Ref. 22.

IV. DISCUSSION

A. Complete fusion and fusion barrier parameters

As discussed in the preceding section the average kinetic energy and the angular distributions of the fission-like events support the interpretation

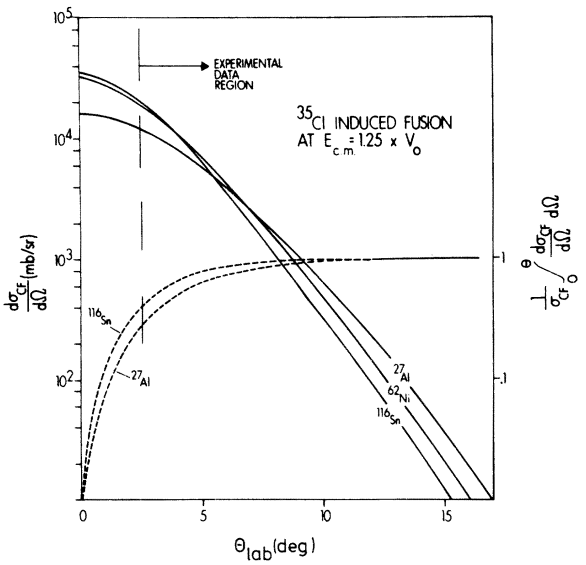

FIG. 4. Smoothed out angular distributions of the evaporation residues for different targets. Projectile energies are 25% above the fusion barrier V_0. The dashed lines refer to the right scale and show the normalized integral contributions of the angular distributions to σ_{CF}.

as fission of an equilibrated system with high angular momentum. Therefore we consider the fission cross section being part of the total fusion cross section:

$$\sigma_{CF} = \sigma_{ER} + \sigma_{FISS} . \tag{1}$$

The excitation function $\sigma_{CF}(E_{c.m.})$ for complete fusion may be analyzed in terms of semiclassical models. Following the potential model of Wong,[24] the cross section for complete fusion is given by

$$\sigma_{CF}(E) = \pi\lambda^2 \sum_{l=0}^{l_{fus}} (2l+1) T(l,E) , \tag{2}$$

where the penetration factor $T(l,E)$ is approximated by the transmission of an inverted parabola[25]

$$T(l,E) = \left(1 + \exp 2\pi \frac{V(R_l) - E}{\hbar\omega_l}\right)^{-1} \tag{3}$$

with $V(R_l)$, R_l, and $\hbar\omega_l$ being the barrier height, position, and curvature for the lth particle wave, respectively. Here, it is assumed that no kinetic energy is lost into internal excitations. If the application of this model is restricted to intermediate energies—i.e., well above the s-wave fusion barrier, so that static deformation effects may be neglected, but not yet in the region where the fusion distance R_l reaches a critical value corresponding to saturation density in the overlap region—both R_l and $\hbar\omega_l$ show only little variation with l. Calculations in the Bass potential model,[9] e.g., for $^{35}Cl + ^{62}Ni$ show that from $l = 10$ to $l = 45$ the fusion barrier increases from 63 to 83 MeV and σ_{CF} for the corresponding to projectile energies from 50 to 700 mb, whereas $\hbar\omega_l$ increases only by 0.5 MeV and R_l decreases by 0.6 fm. Therefore $\hbar\omega_l$ may be approximated by a constant value $\hbar\omega_0$ and R_l within the error limits stated in Table II may be replaced by an average value R_F. Now $V(R_l)$ differs from $V(R_F) = V_F$ only by the centrifugal term $\hbar^2 l(l+1)/2\mu R_F^2$ and Eq. (2) reduces to

$$\sigma_{CF} = \frac{R_F^2 \hbar\omega_0}{2E} \ln\left(1 + \exp 2\pi \frac{E - V_F}{\hbar\omega_0}\right). \tag{4}$$

Well above the barrier V_F the relation $(E - V_F) > \hbar\omega_0$ holds and (4) reduces to the well known sharp cutoff approximation

$$\sigma_{CF}(E) = \pi R_F^2 (1 - V_F/E) . \tag{5}$$

The $1/E_{c.m.}$ dependence predicted by Eq. (5) is confirmed by our data in Figs. 6 and 10 where σ_{CF} is plotted versus $E_{c.m.}^{-1}$. In order to deduce the barrier parameters R_F and V_F from slope and intercept, respectively, Eq. (5) has been fitted to the data. The results are listed in columns 2 and 3 of Table III. Near the fusion barrier, the relation (5) fails to reproduce the experimental results as may be seen for the $^{35}Cl + ^{58,60,62,64}Ni$ data. It has been shown, however, that Eq. (4) can be extended to take static deformations of both, target and projectile, into account.[24] This inclusion of the barrier penetrability and the changes of the fusion barrier height for different orientations of the interacting nuclei with respect to the collision axis allows a consistent description of the $^{35}Cl + Ni$ complete fusion in the barrier region with reasonable values for the parameters $\hbar\omega$ and β (static quadrupole deformation).[4] Furthermore, it turns out that the average barrier heights $\overline{V}_F$ and radii $\overline{R}_F$ of that analysis are not affected and agree with the values deduced with Eq. (5) within the precision of the fit procedure. It should be mentioned, that the barrier height V_F is essentially determined by the relative excitation function and thus should not be influenced by systematic errors, e.g., in the extrapolation of the angular distributions. Because the energy range above the Coulomb barrier is somewhat limited for the Sn targets, the extrapolation of Eq. (5) gives greater uncertainties in values of V_F and R_F than for the lighter targets. This uncertainty is difficult to estimate accurately. Additional data on higher bombarding energies would be most useful for the Sn targets.

In Fig. 7 all but two ($^{35}Cl + ^{54,56}Fe$) excitation functions of this work are presented together with the best fits of Eq. (5); the inserted low energy fit

TABLE II. Summary of evaporation residue cross sections σ_{ER} and fission cross sections σ_{FISS} obtained and used in this study. Critical angular momenta l_{cr} are derived from $\sigma_{CF} = \sigma_{ER} + \sigma_{FISS}$ in the sharp cutoff model.

Reaction	$E_{c.m.}$ (MeV)	σ_{ER} (mb)	$\Delta\sigma_{ER}$(%)	σ_{FISS} (mb)	l_{cr} (σ_{CF})
$^{35}Cl + ^{27}Al$	30.4	15.9	15		3.3
	30.8	32.4	12		4.8
	32.5	128	7		9.8
	39.1	450	5		20
	43.4	637	5		25
	52.1	920	5		33
	56.5	1107	5		38
	62.9	1206	5		42
	69.4	1140 [a]	5		43
	71.6	1170 [a]	10		44
	73.8	1200 [a]	10		45
$^{35}Cl + ^{48}Ti$	57.5	342	5		24
	69.1	668	5		37
	80.6	948	5		48
	92.2	1080	7	60 ± 30	57
$^{35}Cl + ^{54}Fe$	90.5	815	5		48
	96.6	934	5	< 50	53
$^{35}Cl + ^{56}Fe$	63.0	175 [b]	11		19
	64.3	180 [b]	11		20
	73.5	570	20		36
	91.9	1050	7		55
	98.1	964	7	< 50	55
$^{35}Cl + ^{58}Ni$	60.3	6.7	20		2.7
	60.6	10.0	25		3.5
	60.9	18.5	15		5.1
	61.5	31.8	15		7.1
	62.1	46.9	10		8.8
	65.3	143	5		17
	68.4	271	5		24
	74.6	454	5		33
	87.1	781	5		47
$^{35}Cl + ^{60}Ni$	59.2	8.0	25		3.0
	59.5	13.1	25		4.1
	59.8	20.0	15		5.3
	60.5	31.0	15		6.9
	61.4	47.2	15		8.9
	62.4	68.0	10		11
	66.1	210	7		21
	81.6	680	5		43
$^{35}Cl + ^{62}Ni$	59.2	16.1	20		4.7
	59.9	27.6	20		6.5
	60.5	37.3	15		7.8
	60.9	47.6	10		8.9
	61.7	64.9	10		11
	62.4	89	10		13
	63.7	136	5		16
	66.9	268	5		24
	70.1	401	5		30
	76.5	585	5		38
	89.3	929	5		52
	92.4	980	5		55
	102.0	998	5	60 ± 20	61
	105.2	1089	5	90 ± 30	65
	108.4	1091	5	140 ± 45	67

TABLE II. *(Continued)*

Reaction	$E_{c.m.}$ (MeV)	σ_{ER} (mb)	$\Delta\sigma_{ER}$(%)	σ_{FISS} (mb)	$l_{cr}(\sigma_{CF})$
$^{35}Cl+^{64}Ni$	58.6	13.2	20		4.2
	59.2	23.1	20		5.9
	59.9	35.6	15		7.6
	60.5	54.7	10		9.7
	61.2	66.0	10		11
	61.8	89.3	10		13
	63.8	152	7		17
	67.6	328	5		27
	83.8	816	5		49
$^{35}Cl+^{90}Zr$	86.0	86	15		17
	88.1	129	10		21
	89.6	190	7		26
	93.3	286	7		32
	98.2	478	7		42
	103.3	576	5		48
	118.4	850	5		62
$^{35}Cl+^{116}Sn$	107.1	141	15		24
	110.1	211	7		31
	114.7	327	5		38
	122.4	446	5	40±15	49
	126.4			90±30 [c]	(54)
	130.1	560	7	135±45	61
$^{35}Cl+^{124}Sn$	108.9	136	15		24
	112.0	225	7		32
	116.7	352	7		40
	124.5	490	7		49
	128.4			25±10 [c]	(55)
	132.3	632	5	60±20	62

[a] Including fission contributions.
[b] Taken from Ref. 20.
[c] Reference 22.

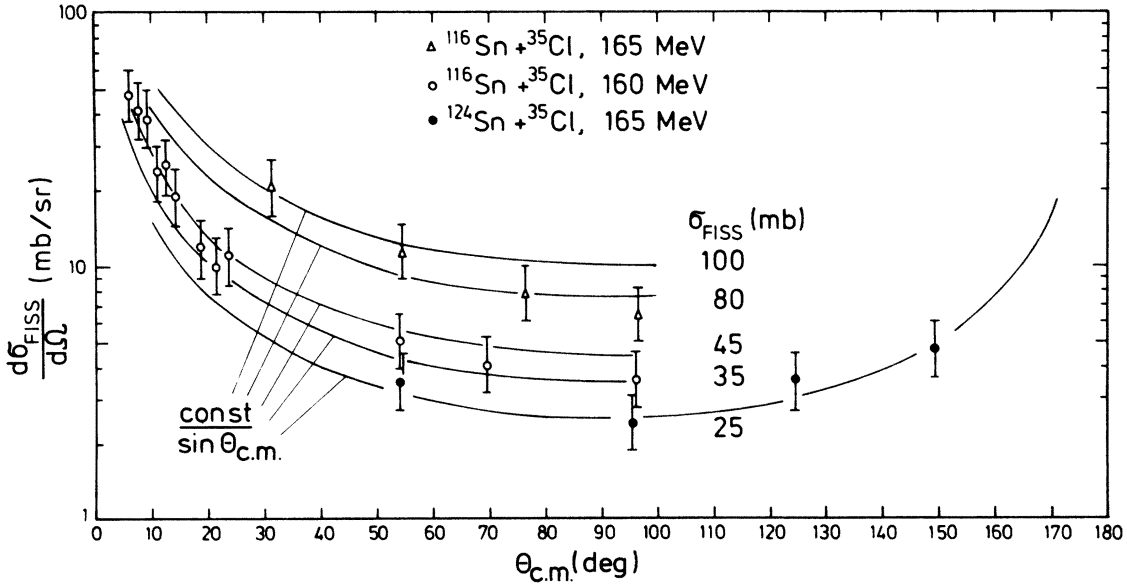

FIG. 5. Angular distributions of fission-like events for $^{35}Cl+^{116,124}Sn$ at 160 and 165 MeV. Conversion into the center of mass system was done assuming symmetric binary fission. Solid lines show the $(\sin\theta_{c.m.})^{-1}$ dependence expected for fission of equilibrated systems.

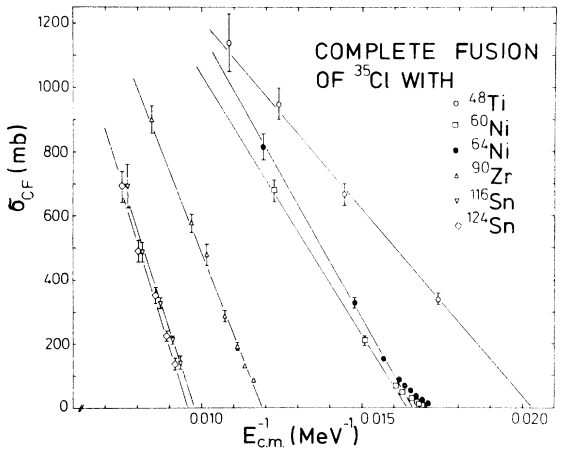

FIG. 6. Complete fusion cross sections versus $1/E_{c.m.}$. Solid lines are fits of Eq. (5). The parameters are listed in Table III.

for ^{35}Cl + Ni is taken from Ref. 4. The overall agreement is very satisfying so that we may now have a closer look at the barrier parameters extracted by means of this simple semiclassical picture.

The fusion radii R_F roughly follow a mass dependence $R_F = r_0(A_T^{1/3} + A_P^{1/3})$ with r_0 decreasing from 1.34 fm (^{27}Al) to 1.21 fm (^{116}Sn). This dependency of r_0 on the combined mass number $A_T^{1/3} + A_P^{1/3}$ (or $Z_P Z_T$) indicates that for the systems under study the nuclear density overlap at the fusion point slowly increases with increasing mass number. Taking the half density radii and diffuseness $a = 0.57$ fm from electron scattering results[26,27] as was done for Fig. 8, the density in units of the saturation density varies between 0.15 (^{27}Al, ^{64}Ni) and 0.27 (^{116}Sn); this is slightly more than for the ^{32}S-induced fusion[3] with ^{24}Mg, ^{27}Al, and ^{40}Ca, where relative densities of 0.11–0.15 follow from the radii listed in Table III. For $R < R_F$ the one dimensional potential barrier for s waves

$$V(R) = V_{Coul}(R) - V_{Nucl}(R) < V(R_F) \qquad (6)$$

bends down, because the attractive nuclear forces dominate; i.e., the onset of fusion is located in the nuclear surface regions $\rho \approx 0.15$–$0.25\rho_0$.

Within the sequence of Ni isotopes and, less pronounced, for ^{116,124}Sn the fusion radii show a stronger increase with mass number than is expected from the gross mass dependence. It also exceeds the increase of the half density charge distribution radii[26] with mass number within the isotopic sequence by a factor of about 3. This seems to be an effect of adding neutrons to a closed shell configuration ^{56}Ni. It is interesting to note, that from total reaction cross sections σ_R for 30–60 MeV protons on ^{58,60,62,64}Ni a comparably strong dependence of the radius parameter R in $\sigma_R = \pi(R + \lambda)^2$, where λ is the de Broglie wave length, on the neutron excess has been observed.[28]

Similar observations have been made by Tabor, Watson, and Hanna[29] and Boyd *et al.*[30] who found that the matter radii of even tin isotopes from elastic p, α, and ^{16}O scattering increase a factor of 2–3 more rapidly with neutron number than do the charge distribution radii.

We now focus attention on the fusion barrier V_F. The experimental values in Table III roughly in-

TABLE III. Parameters R_F (in fm) and V_F (in MeV) of fusion barriers deduced from a fit of Eq. (5)— for ^{35}Cl + Ni: Eq. (4) — to the experimental complete fusion excitation functions, and from potential model calculations, respectively.

			Calculations							
	Experiment		Bass (Ref. 9) [a]		Krappe *et al.* (Ref. 13)		Ngô *et al.* (Ref. 10)		Wilszynski *et al.* (Ref. 12)	
Reaction	R_F	V_F	R_F	V_F	R_F	V_F	R_F	V_F	R_F	V_F
^{35}Cl + ^{27}Al	8.4 ± 0.2	30.7 ± 0.4	9.38 (8.98)	29.0 (30.1)	8.85	31.0	9.1	32.4	9.12	31.3
^{35}Cl + ^{48}Ti	8.7 ± 0.3	49.2 ± 0.6	9.51 (9.22)	48.6 (49.9)	9.30	50.3	9.6	52.1	9.83	49.1
^{35}Cl + ^{56}Fe	9.5 ± 0.4	59.5 ± 1.0	9.54 (9.28)	57.3 (58.6)	9.43	58.7	9.8	60.4	9.99	57.0
^{35}Cl + ^{58}Ni	9.0 ± 0.2	61.3 ± 0.3	9.47 (9.19)	62.0 (63.6)	9.45	63.2	9.8	64.9	9.97	61.4
^{35}Cl + ^{60}Ni	9.2 ± 0.2	61.0 ± 0.3	9.55 (9.28)	61.6 (63.1)	9.50	62.8	9.8	64.6	10.07	60.9
^{35}Cl + ^{62}Ni	9.6 ± 0.2	60.8 ± 0.3	9.62 (9.36)	61.2 (62.7)	9.56	62.5	9.9	64.2	10.15	60.5
^{35}Cl + ^{64}Ni	9.7 ± 0.2	60.3 ± 0.3	9.69 (9.44)	60.9 (62.2)	9.63	62.2	10.0	63.8	10.22	60.0
^{35}Cl + ^{90}Zr	9.8 ± 0.3	84.0 ± 0.5	9.83 (9.63)	85.9 (87.4)	9.97	86.1	10.4	87.7	10.62	82.5
^{35}Cl + ^{116}Sn	9.8 ± 0.4	102.3 ± 0.9	10.06 (9.91)	105.3 (106.7)	10.25	105.0	10.8	105.8	11.00	99.6
^{35}Cl + ^{124}Sn	10.1 ± 0.4	104.0 ± 0.8	10.24 (10.10)	103.8 (105.0)	10.35	104.1	11.0	104.4	11.19	98.1
^{32}S + ^{24}Mg [b]	8.5 ± 0.3	27.8 ± 0.3	9.27 (8.83)	25.5 (26.5)	8.67	27.4	8.9	29.1	8.83	28.1
^{32}S + ^{27}Al [b]	8.3 ± 0.3	29.2 ± 0.2	9.32 (8.91)	27.5 (28.5)	8.75	29.5	9.0	31.2	9.00	29.9
^{32}S + ^{40}Ca [b]	9.0 ± 0.3	43.2 ± 0.2	9.26 (8.91)	42.5 (43.9)	9.02	44.1	9.3	46.0	9.38	44.0

[a] Using $r_0 = 1.07$ fm. In parentheses: Using Elton's (Ref. 27) half density radii.
[b] Analysis of data from Ref. 3.

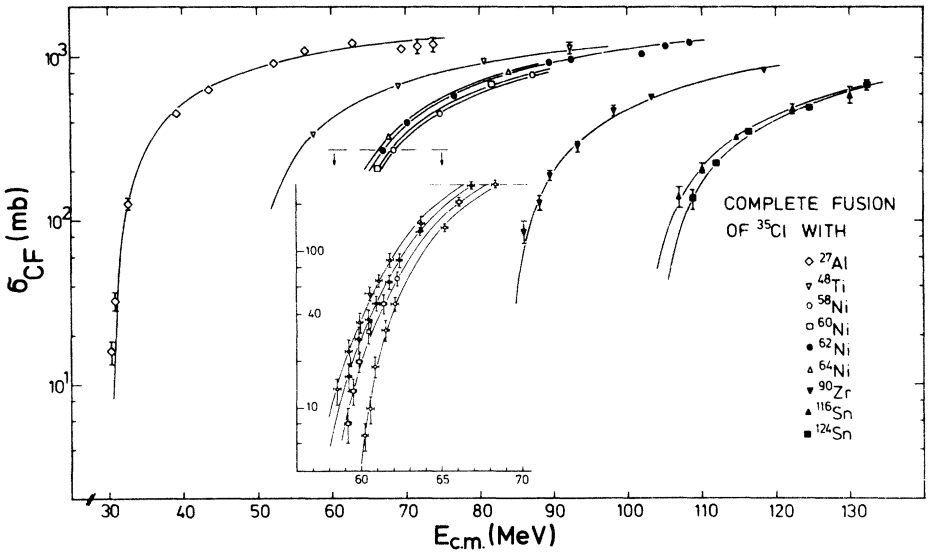

FIG. 7. Complete fusion excitation functions. Solid lines are best fits of Eq. (5). The inserted low energy fit to the ^{35}Cl+Ni data is taken from Ref. 4 and includes the effects of barrier penetration and static quadrupole deformation.

crease proportional to $Z_P Z_T$. Within a sequence of isotopes V_F is expected to decrease with increasing mass. The ^{35}Cl+Ni barriers follow this trend, whereas the two tin isotopes show the opposite behavior; however, additional data on more tin isotopes are needed before conclusions can be drawn.

Comparing the experimental V_F values with the Coulomb potential taken at the distance R_F the difference

$$V_N(R_F) = V_F - \frac{Z_P Z_T e^2}{R_F}, \tag{7}$$

which may be interpreted as nuclear contribution to the barrier for s waves at the distance R_F neglecting all dynamical deformations, is in the order of 20% of the Coulomb part and increases as a function of $Z_P Z_T$ as is shown in Fig. 9.

B. Comparison with model calculations

In the past few years the increasing interest in the reaction mechanism of the different categories of interactions between heavy ions has led to the development of several new models.[9-16] Because of the large number of degrees of freedom involved and the high excitations obtainable it is almost impossible to describe fusion- and fission-like processes in a microscopic model. Instead, statistical descriptions for the equilibrated system are used[17] and the equilibration itself is described in terms of semiclassical and classical models that reduce the number of degrees of freedom by introducing macroscopic concepts like friction and simplifying assumptions, e.g., the sudden approximation. Most of these models are one dimensional potential models using the distance between the centers of mass of the colliding ions as dynamical variable. For a comprehensive survey of these phenomenological heavy ion interac-

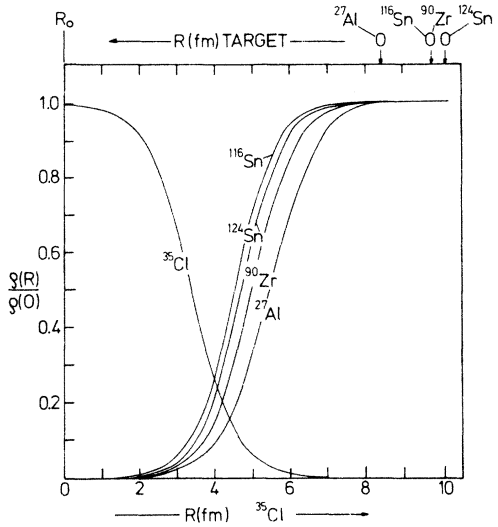

FIG. 8. Nuclear density overlap at the fusion barrier. Plotted from left to right: Relative charge density distribution of ^{35}Cl; from right to left: Relative charge density distribution of different targets. Charge densities are based on electron scattering data analysis (Ref. 27). The radial distance R_0 of the interacting ions is the fusion radius.

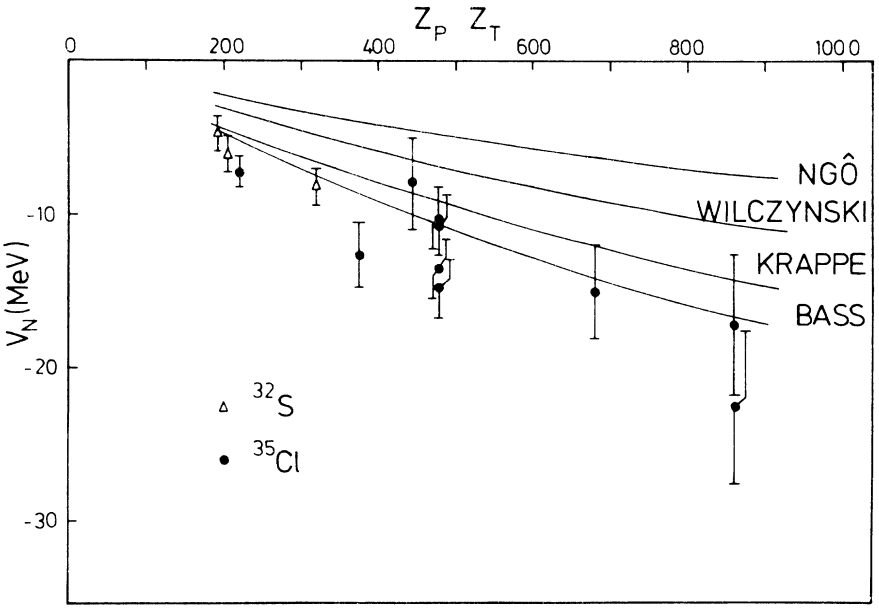

FIG. 9. Nuclear part of the fusion barrier versus $Z_P Z_T$. The ^{32}S data are taken from Ref. 3. Solid lines are predictions of the different model potentials (Refs. 9–13).

tion potentials the reader is referred to the review article of Krappe.[31] In the following subsections we compare the predictions of some representative models with experimental results, both from the literature and from this study.

1. *Fusion barrier heights and radii*

Following Wong[32] the fusion barrier is equal to the height of the potential barrier $V_F = V(R_F)$ for head on collision and the fusion radius R_F is the corresponding radial distance:

$$\left.\frac{dV(R)}{dR}\right|_{R=R_F} = 0 . \tag{8}$$

The energy density formalism has been applied by Ngô *et al.*[10,11] to calculate the interaction potential $V(R)$ in the sudden approximation assuming spherical symmetry for both colliding ions. The model makes use of nuclear density distributions taken from Hartree-Fock calculations. It contains no additional parameters adjusted for fusion calculations. The potential maximum V_F defined by Eq. (8) can be interpreted as fusion barrier, if the additional relation $V_F > V(R_{cr})$ holds. Here, $R_{cr} < R_F$ is the critical distance of approach,[33] that is defined as the distance where the initial kinetic energy in the center of mass system is converted into potential energy for an interaction with the critical angular momentum. Galin *et al.*[33] have shown that $R_{cr} = r_0(A_T^{1/3} + A_P^{1/3})$ with $r_0 = (1.0 \pm 0.07)$ fm for a broad range of heavy ions and energies. The requirement $V_F > V(R_{cr})$ is generally fulfilled if $Z_P Z_T < 1700$, i.e., for all systems considered here. This model is expected to predict the fusion barriers to within ±3%.

The results are listed in Table III. The calculated fusion barrier heights V_F turn out to be systematically higher than the experimental data. The differences decrease from about 5% for the light systems to less than 3% for the ^{35}Cl + ^{116,124}Sn results. The fusion radii predicted are also greater than the experimental values. Ngô's model assumes that fusion will occur if the critical distance R_{cr} can be reached by the interacting ions. As R_{cr} is smaller than R_F, the nuclear contribution $V_N(R_F)$ to the fusion barrier calculated with Eq. (7) is expected to be fairly small. The comparison of the calculated $V_N(R_F)$ with the values deduced from our experimental data (Fig. 9) shows that Ngô's model predicts too low a nuclear density overlap at the distance R_F.

Wilczyński and Siwek-Wilczyńska[12] have proposed a potential whose parameters are derived from boundary conditions. It is composed of a real nuclear part of spherical Woods-Saxon shape and a Coulomb part that at large separations is identical with the point charge approximation and at small distances approaches a constant value. Near the fusion radius R_F this Coulomb part deviates from the point charge approximation by typically 0.6%. The speed of this approach is con-

trolled by the only free parameter of the model; it was adjusted to reproduce experimentally determined fusion barriers over a broad range of energies and masses.

The results in Table III show a good agreement as far as the fusion barrier heights for the lighter systems are concerned. The fusion radii are very similar to those of the Ngo potential resulting again in a low value for the nuclear part V_N of the barrier as shown in Fig. 9.

The model of Krappe and Nix[13] is based on the liquid drop model with modification to account for the finite range of the nuclear interaction. The four parameters involved, including a range parameter a of the nuclear potential, have been determined by adjustment to experimental fission and interaction barrier heights. The results of this model are presented in Table III. Excellent overall agreement can be stated for both barrier heights and fusion radii. This agreement may be expressed in terms of the fusion distance d defined by[13]

$$V_F = \frac{Z_P Z_T e^2}{r_0(A_P^{1/3} + A_T^{1/3}) + a + d}\,, \tag{9}$$

where $r_0 A^{1/3}$ with $r_0 = 1.16$ fm is the equivalent sharp radius,[34] and $a = 1.4$ fm is the nuclear force range parameter. From $R_F = r_0(A_P^{1/3} + A_T^{1/3}) + d$ it follows that d is the distance of the sharp nuclear surfaces at the fusion barrier of Eq. (8). Applying Eq. (9) to the experimental values for V_F yields the fusion distances listed in Table IV together with the theoretical predictions. The decrease of d with increasing $Z_P Z_T$ corresponds to the increasing density overlap stated earlier.

In the model of Bass[9] formulated for spherical nuclei the attractive nuclear force is related to the specific surface energy of the liquid drop model. The nuclear radii are identified with the half density radius and $R_{12} = r_0(A_P^{1/3} + A_T^{1/3})$ is either calculated with the radius parameter $r_0 = 1.07$ fm or taken from Elton's[27] fit to the half density radii from electron scattering:

$$r_0 = (1.123 - 0.941A^{-2/3})\ \text{fm}\,. \tag{10}$$

R_{12} is interpreted as the radial distance that must be reached before dissipation of energy and angular momentum can take place and fusion may occur. In this respect R_{12} is to be compared with the critical distance R_{cr} of Ref. 33. Fusion radii and barrier heights derived from this potential by means of Eq. (8) are listed in Table III. The agreement is satisfactory, especially if r_0 is taken from Eq. (10).

A comparison of the model predictions shows that the two liquid drop models work best. This is confirmed by the nuclear contributions V_N to the potential derived with Eq. (7) and presented in Fig. 9. This is in part due to the fact that the inherent parameters were adjusted to reproduce barrier heights. Because of its simple analytical expressions the Bass model represents a quick and reliable tool to calculate fusion barrier heights and radii. Comparison of some of our data with the model of Gross and Kalinowski[14] has been presented in Ref. 35.

TABLE IV. The fusion distance d (in fm) calculated from the liquid drop model (Ref. 13) and from the experimental fusion barrier V_F by means of Eq. (9) with $r_0 = 1.16$ fm and $a = 1.40$ fm.

Reaction	Experiment	Liquid drop model
^{35}Cl + ^{27}Al	1.68	1.60
^{35}Cl + ^{48}Ti	1.53	1.30
^{35}Cl + ^{56}Fe	1.06	1.20
^{35}Cl + ^{58}Ni	1.49	1.15
^{35}Cl + ^{60}Ni	1.49	1.15
^{35}Cl + ^{62}Ni	1.48	1.10
^{35}Cl + ^{64}Ni	1.52	1.10
^{35}Cl + ^{90}Zr	1.26	0.95
^{35}Cl + ^{116}Sn	1.11	0.80
^{35}Cl + ^{124}Sn	0.77	0.75
^{32}S + ^{24}Mg [a]	1.51	1.65
^{32}S + ^{27}Al [a]	1.69	1.60
^{32}S + ^{40}Ca [a]	1.61	1.40

[a] Taken from Ref. 3.

2. *Interaction and fusion barriers*

The fusion barrier as defined by Eq. (8) for the systems under study has been located in the region of about 20% nuclear density overlap. Nuclear interactions, e.g., quasielastic and transfer processes, however, start when the overlap is much less.[12,15] This separation, the interaction radius R_{INT}, therefore should exceed the fusion radius by an amount in the order of 2 times the nuclear surface diffuseness, i.e., 1–2 fm. Accordingly, the interaction barrier should be almost identical with the Coulomb potential V_C (R_{INT}).

Interaction radii and total reaction cross sections σ_R have been determined from elastic scattering of ^{35}Cl with ^{58,62}Ni and ^{116,124}Sn at energies between 120 and 170 MeV with the quarter point method. Only the reaction cross sections for ^{35}Cl + ^{58,62}Ni at $E_{lab} = 100$ MeV have been taken from the full optical model analysis (Sec. IIIA). In the sharp cutoff approximation σ_R is related to R_{INT} and V_{INT} by the counterpart of Eq. (5), namely,

$$\sigma_R(E) = \pi R_{INT}^2 (1 - V_{INT}/E_{c.m.})\,. \tag{5'}$$

Applying Eq. (5′) to the reaction cross sections from Ref. 22 and from Fig. 2 yields the interaction barrier parameters shown in Fig. 10 and listed in

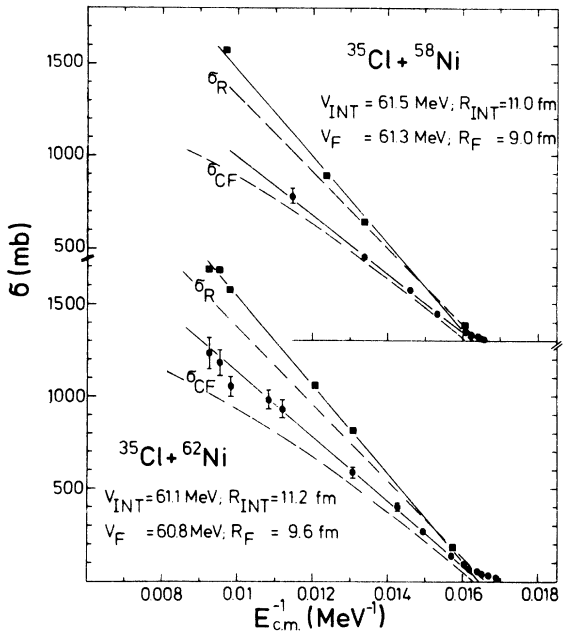

FIG. 10. Total reaction and complete fusion cross sections versus $1/E_{c.m.}$. Solid squares are cross sections from Ref. 22 with exception of the ones near 0.016 MeV^{-1}; see Fig. 2. The parameters are extracted from the fits of Eqs. (5) and (5′). Dashed lines: predictions of the Bass model using Elton's half density radii for R_{12}.

Table V. A comparison with the fusion data shows, that for the lighter systems $V_{INT} \approx V_F$, whereas for $^{35}Cl + ^{116,124}Sn$ and heavier systems like $^{40}Ar + ^{109}Ag$ (Ref. 6), $V_F - V_{INT} > 0$ in agreement with earlier predictions, e.g., of the Bass model.[9] Also, the interaction radii turn out to be 1.5–2.4 fm higher than the fusion radii in support of the speculation given at the top of this subsection.

For the systems with $V_{INT} \approx V_F$ it follows from Eqs. (5) and (5′) that

$$\sigma_{CF}/\sigma_R \approx (R_F/R_{INT})^2 , \qquad (11)$$

i.e., the fraction of the reaction cross section that goes into complete fusion is not sensitive to the energy in the energy region $E > V_F$, as may be seen from Fig. 10. The missing part $(\sigma_R - \sigma_{CF})$ is in the order of 25–35% of the total reaction cross section in agreement with the results for the systems $^{12}C + ^{152}Sm$, $^{16}O + ^{150}Nd$, and $^{18}O + ^{148}Nd$ at comparable energies.[8] With increasing mass number the ratio σ_{CF}/σ_R drops below the value of Eq. (11), because the difference between the fusion and the interaction barrier heights increases. These results contradict the phenomenological model for complete fusion cross section in heavy ion reaction recently proposed[37] which starts from the assumption that for projectiles with energies less than 4 MeV nucleon above the Coulomb barrier σ_{CF} almost equals the reaction cross section σ_R.

The difference between σ_R and σ_{CF} is assumed to go into inelastic and direct transfer reactions. For $^{62}Ni + ^{35}Cl$ at $E_{lab} = 100$ MeV we find from Fig. 2 that $\sigma_R - \sigma_{trans} = 159$ mb, if σ_R is taken from the optical model analysis. This is in reasonable agreement with $\sigma_{CF} = 136$ mb (Table II). At these energies near the barrier the quarter point method yields total reaction cross sections that are too small[38]; for $^{62}Ni + ^{35}Cl$ we get $\sigma_R(\Theta_{1/4}) = 109$ mb, and the $^{35}Cl + ^{58}Ni$ elastic scattering angular distribution does not reach the quarter point (Fig. 2).

Finally, it should be pointed out again, that barrier penetrability and deformation effects are not included in the potential models and analyses discussed. Therefore we consider V_F, R_F, V_{INT}, and R_{INT} as average barrier values. The inclusion of these effects, however, is supposed to introduce only small modifications.[4,36] The evaporation residue cross sections near the barrier, however, are very sensitive to static quadrupole deformations.[4] With the sources for negative polarized heavy ions becoming available[39] experiments to study the influence of deformations on the fusion barrier in detail may prove feasible.[40]

3. *Angular momentum cutoffs, fission, and evaporation residue excitation functions*

The simultaneous measurement of evaporation residue (ER) and fission excitation functions al-

TABLE V. Comparison of interaction and fusion barrier parameters.

Reaction	R_F (fm)	V_F (MeV)	R_{INT} [a] (fm)	R_{INT} [b] (fm)	V_{INT} [a] (fm)	$(R_F/R_{INT})^2$
$^{35}Cl + ^{27}Al$	8.4	30.7	···	9.9	31.4	0.71
$^{35}Cl + ^{58}Ni$	9.0	61.3	11.0	11.0	61.5	0.66
$^{35}Cl + ^{62}Ni$	9.6	60.8	11.2	11.2	61.1	0.73
$^{35}Cl + ^{116}Sn$	9.8	102.3	···	12.2	99.8	0.64
$^{35}Cl + ^{124}Sn$	10.1	104.0	···	12.4	98.7	0.66

[a] From Eq. (5′).
[b] From Ref. 22.

lows an estimation of the critical angular momentum limits for fission. These data may then be used as a test of the rotating liquid drop model with respect to fissionability as a function of excitation energy and angular momentum J. This point is particularly interesting in view of current interest in shapes of nuclei at very high angular momenta; the enhanced fissionabilities at high J result from the accompanying deformation.

The rotating drop model is also of interest in its ability or inability to predict the limits with projectile energy of evaporation residue cross sections. This is relevant to the question as to whether the ER cross section limits result from entrance conditions or from the ability of high partial waves to survive fission.

The simplest approach to estimating the critical angular momenta for fusion is application of the sharp cutoff model to the sums of the experimental ER and fission cross sections. We have followed this procedure by setting $T(l,E)=1$ in Eq. (2) for $l \leq l_{cr}$ and 0 above, and summarize the sharp cutoff values l_{cr} in Table II. It is most unlikely that nature gives precisely such a sharp cutoff; if not, values of l_{cr} greater than those given by the sharp cutoff model (SCM) are allowed in the fusion cross section [but with $T(l,E)<1$]. Clearly the SCM gives a lower limit to l_{cr}; however, at present we do not feel that there is satisfactory evidence to provide a better estimate of the high angular momentum limit.

With this uncertainty we have performed statistical model calculations for the excitation functions shown in Fig. 11 using the computer code OVERLAID ALICE,[41] a revised and improved version of the code ALICE.[17,42] These codes use the rotating liquid drop model parameters of Cohen, Plasil, and Swiatecki[43] in an angular-momentum-dependent Bohr-Wheeler fission-evaporation competition calculation.[44] As details of the calculation have been described in Ref. 17, and since the codes have been widely distributed and used, we present a minimal discussion of parameters in this work.

For the ^{62}Ni and ^{116}Sn targets the number of partial waves in the evaporation/fission calculations was limited to the sharp cutoff values summarized in Table II. For the ^{27}Al target, for which the fission excitation function was not measured, all partial waves of the reaction cross section as given by the parabolic model were included in the calculation. The ratio of single particle level densities at the saddle point to those for the equilibrium rotating charged drop (a_f/a_n) was taken to be 1.0 for one set of calculations. A second set of results were computed for ^{116}Sn+^{35}Cl with a_f/a_n

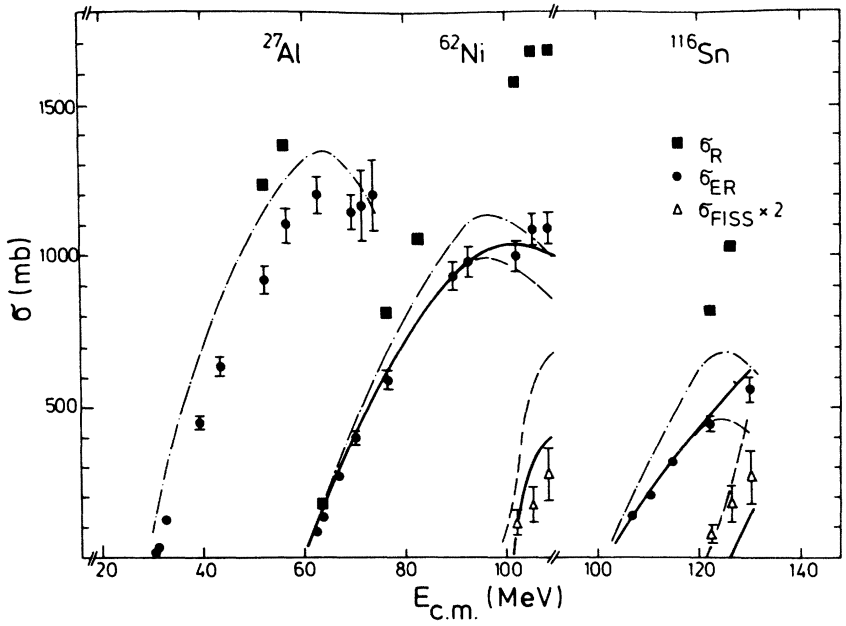

FIG. 11. Experimental and calculated reaction, evaporation residue, and fission excitation functions. Dash-dotted curves: ER excitation functions for $a_f/a_n=1$ taking into account all partial waves. Solid lines: ER and fission excitation functions for $a_f/a_n=1$ in the sharp cutoff model, restricting the partial waves to $l \leq l_{cr}$ from Table II. Dashed lines: Excitation functions in the SCM with $a_f/a_n=1.2$ (^{35}Cl+^{62}Ni) and $a_f/a_n=1.25$ (^{35}Cl+^{116}Sn), respectively. All fission data and calculations are multiplied by a factor 2. The three high energy cross sections σ_{ER} for ^{27}Al+^{35}Cl include fission contributions (see Table II).

$= 1.25$ and for $^{62}Ni + ^{35}Cl$ with $a_f/a_n = 1.20$. It may be seen in Fig. 11 that within these reasonable parameter limits both the ER and fission excitation functions may be reasonably reproduced. This in turn implies that the deformations at high angular momenta which are given by the rotating liquid drop model are consistent with these experimental results. It does not prove that they are unique. Caution must also be shown since the experimental yields which are treated here as fission events may include contributions from processes which are not due to equilibrium fission. More careful analysis of angular and mass distributions of these products is required before concluding that the yields are or are not consistent with an equilibrium fission mechanism.[22]

V. CONCLUSIONS

The experimental measurements of this work permit an estimation of the radii and barrier heights for fusion as a function of target atomic number. It is found that the density overlap required for fusion increases with increasing target atomic number, as expected from simple theoretical considerations. Similarly the nuclear attractive component of the fusion barrier is shown to increase with target atomic number. We find an increasing difference between fusion barrier and interaction barrier heights with target atomic number, and a correspondingly lower percentage of the reaction cross section undergoing fusion. All these observations may be qualitatively understood in terms of one dimensional potential energy curves; a quantitative theoretical understanding may require consideration of multidimensional potential energy surfaces.[45] We hope that experiments of the type reported herein will provide the data necessary for developing models by which the fusion and nonfusion portions of heavy ion reaction cross sections can be understood.

The ER cross section limits at the higher bombarding energies (for which fission-like processes are observed) are reproduced reasonably well by the fission/evaporation model which we have used. At lower bombarding energies the deviation between ER and reaction cross sections must be attributed entirely to noncompound processes.

The authors wish to acknowledge the support and encouragement obtained at Brookhaven National Laboratory, especially from A. Z. Schwarzschild and H. E. Wegner.

---

*Work supported in part by U.S.E.R.D.A.
†Supported by the National Science Foundation.
‡Present address: Lawrence Berkeley Laboratory, Berkeley, California 94720.

[1]J. D. Garrett, H. E. Wegner, T. M. Cormier, E. R. Cosman, and A. J. Lazzarini, Phys. Rev. C 12, 481 (1975).
[2]R. L. Kozub, N. H. Lu, J. M. Miller, D. Logan, T. W. Debiak, and L. Kowalski, Phys. Rev. C 11, 1497 (1975).
[3]H. H. Gutbrod, W. G. Winn, and M. Blann, Nucl. Phys. A213, 267 (1973).
[4]W. Scobel, A. Mignerey, M. Blann, and H. H. Gutbrod, Phys. Rev. C 11, 1701 (1975).
[5]T. M. Cormier, E. R. Cosman, A. J. Lazzarini, J. D. Garrett, and H. E. Wegner, Phys. Rev. C 14, 334 (1976).
[6]H. C. Britt, B. Erkkila, R. H. Stokes, H. H. Gutbrod, F. Plasil, R. L. Ferguson, and M. Blann, Phys. Rev. C 13, 1483 (1976).
[7]A. M. Zebelman, L. Kowalski, J. Miller, K. Beg, Y. Eyal, G. Jaffe, A. Kandil, and D. Logan, Phys. Rev. C 10, 200 (1974).
[8]R. Broda, M. Ishihara, B. Herskind, H. Oeschler, and S. Ogaza, Nucl. Phys. A248, 356 (1975).
[9]R. Bass, Phys. Lett. 47B, 139 (1973); Nucl. Phys. A231, 45 (1974).
[10]C. Ngô, B. Tamain, J. Galin, M. Beiner, and R. J. L. Lombard, Nucl. Phys. A240, 353 (1975).
[11]C. Ngô, B. Tamain, M. Beiner, R. J. L. Lombard, D. Mas, and H. H. Deub, Nucl. Phys. A252, 237 (1975).
[12]J. Wilczyński and K. Siwek-Wilczyńska, Phys. Lett. 55B, 270 (1975).
[13]H. J. Krappe and J. R. Nix, in *Proceedings of the Third International Atomic Energy Symposium on the Physics and Chemistry of Fission, Rochester, 1973* (International Atomic Energy Agency, Vienna, 1974), p. 159.
[14]D. H. E. Gross and H. Kalinowski, Phys. Lett. 48B, 302 (1974).
[15]D. M. Brink and N. Rowley, Nucl. Phys. A219, 79 (1974).
[16]R. Da Silveira, Phys. Lett. 50B, 237 (1974).
[17]F. Plasil and M. Blann, Phys. Rev. C 11, 508 (1975).
[18]H. H. Gutbrod, M. Blann, and W. G. Winn, Nucl. Phys. A213, 285 (1973).
[19]P. Thieberger, H. E. Wegner, M. McKeown, M. Manni, and I. Feigenbaum, Nucl. Instrum. Methods 122, 291 (1974).
[20]M. Hille and P. Hille (private communication).
[21]V. E. Viola, Jr., Nucl. Data 1, 391 (1966).
[22]J. Bisplinghoff, M. Blann, A. Mignerey, P. David, J. Ernst, T. Mayer-Kuckuk, and W. Scobel, Bull. Am. Phys. Soc. 21, 656 (1976); J. Bisplinghoff, W. Scobel, M. Blann, P. David, J. Ernst, T. Mayer-Kuckuk, A. Mignerey, M. Beckermann, and O. Zohni, Report No. COO-3494-31, 1976 (unpublished).
[23]R. Vandenbosch and J. R. Huizenga, *Nuclear Fission* (Academic, New York, 1973).
[24]C. Y. Wong, Phys. Rev. Lett. 31, 766 (1973).
[25]D. L. Hill and J. A. Wheeler, Phys. Rev. 89, 1102 (1953).
[26]C. W. De Jager, H. DeVries, and C. DeVries, At. Data

Nucl. Data Tables 4, 479 (1974).
[27]H. Überall, *Electron Scattering from Complex Nuclei* (Academic, New York, 1971), Sec. 3, p. 213.
[28]J. J. Menet, E. E. Gross, J. J. Malanify, and A. Zucker, Phys. Rev. C 4, 1114 (1971).
[29]S. L. Tabor, B. A. Watson, and S. S. Hanna, Phys. Rev. C 11, 198 (1975).
[30]R. N. Boyd, J. Fenton, M. Williams, T. Kruse, and W. Savin, Nucl. Phys. A162, 497 (1971).
[31]H. J. Krappe, in *Proceedings of the Symposium on Classical and Quantum Mechanical Aspects of Heavy Ion Collisions, Heidelberg, Germany, 1974* (Springer, Berlin, 1975).
[32]C. Y. Wong, Phys. Lett. 42B, 186 (1972).
[33]J. Galin, D. Guerreau, M. Lefort, and X. Tarrago, Phys. Rev. C 9, 1018 (1974).
[34]W. D. Myers, Nucl. Phys. A204, 465 (1973).
[35]D. H. E. Gross, H. Kalinowski, and J. N. De, in *Proceedings of the Symposium on Classical and Quantum Mechanical Aspects of Heavy Ion Collisions, Heidelberg, Germany, 1974* (see Ref. 31).
[36]J. M. Alexander, L. C. Vaz, and S. Y. Lin, Phys. Rev. Lett. 33, 1487 (1974).
[37]E. Seglie and D. Sperber, Phys. Rev. C 12, 1236 (1975).
[38]N. Rowley and E. Plagnol, Phys. Lett. 56B, 221 (1975).
[39]E. Steffens, in *Proceedings of the International Conference on Heavy Ion Sources, Gatlinburg, 1975* [IEEE Trans. Nucl. Sci. NS-23, 1145 (1976)].
[40]D. Fick, in *Proceedings of the Fourth International Symposium on Polarization Phenomena in Nuclear Reactions, Zürich, 1975* (Birkhäuser, Basel, 1976), p. 357.
[41]M. Blann, OVERLAID ALICE, a statistical model computer code including fission and preequilibrium models, U.S. Atomic Energy Commission Report No. COO-3494-29, 1976 (unpublished).
[42]M. Blann and F. Plasil, ALICE, a nuclear evaporation code, U.S. Atomic Energy Commission Report No. COO-3494-10, 1973 (unpublished).
[43]S. Cohen, F. Plasil, and W. J. Swiatecki, Ann. Phys. (N. Y.) 82, 557 (1974).
[44]N. Bohr and J. A. Wheeler, Phys. Rev. 56, 426 (1939).
[45]O. Zohni and M. Blann, Bull. Am. Phys. Soc. 21, 675 (1976).